How to cite: *Angew. Chem. Int. Ed.* **2025**, *64*, e202413584
doi.org/10.1002/anie.202413584

Solar Cells

A-Site Engineering with Thiophene-Based Ammonium for High-Efficiency 2D/3D Tin Halide Perovskite Solar Cells

Guitao Feng, Hok-Leung Loi, Tianyue Wang, Wenqiu Deng, Zhiqiang Guan, Qi Wei, Jiandong He, Mingjie Li, Chun-Sing Lee, Jizheng Wang, Qichun Zhang,* and Feng Yan**

Abstract: Tin halide perovskites are the most promising candidate materials for lead-free perovskite solar cells (PSCs) thanks to their low toxicity and ideal band gap energies. The introduction of 2D/3D mixed perovskite phases in tin-based PSCs (TPSCs) has proven to be the most effective approach to improving device efficiency and stability. However, a 2D perovskite phase normally shows relatively low carrier mobility, which will be unfavorable for carrier transfer in the devices. In this work, we used a thiophene-based cation 2-(thiophen-3-yl)ethan-1-aminium (3-TEA) as a spacer to form a novel 2D perovskite phase in TPSCs, which shows the most promising effect on the performance enhancement in comparison with other cations like 2-(thiophen-2-yl)ethan-1-aminium (2-TEA) and benzene-based 2-phenylethan-1-aminium (PEA). Theoretical calculations reveal that 3-TEA enables the most compact crystal packing of $[SnI_6]^{4-}$ octahedral layers, resulting in the lowest hole effective mass and formation energy in the 2D phase. This effect significantly enhances device efficiency and stability by facilitating more efficient carrier transfer within the 2D phase. These findings indicate that thiophene-based 2D perovskites are well-suited for high-performance TPSCs.

Introduction

Perovskite solar cells (PSCs) have attracted considerable attention in recent years due to their exceptional photovoltaic performance and cost-effective manufacturing, which have been recognized as a promising next-generation photovoltaic technology.[1] However, the most promising PSCs are based on lead (Pb) halide perovskites, which pose significant risks to the ecological environment even with minimal toxic lead emissions.[2] To address this concern, tin-based perovskite solar cells have been developed due to the similar outer electronic configurations and ionic radius of Sn^{2+} to Pb^{2+}, as well as the suitable energy band gap of tin-based perovskites, which falls within the optimal range defined by the Shockley–Queisser limit.[2a,3] However, the elevated energy level of Sn-5 s orbitals makes Sn^{2+} susceptible to oxidation, while the rapid crystallization rate of tin-based perovskite complicates the control of film quality and morphology, further impacting the photovoltaic properties.[4] To overcome these drawbacks, reducing agents, such as SnF_2,[5] $SnCl_2$,[6] PHCl,[7] KHQSA,[8] GA,[9] 8-HQ,[10] hydrazine,[11] and halogenated hydrazine salts,[12] have been introduced as additives to prohibit the oxidation of Sn^{2+}. Another strategy is to introduce large organic ligands into the A-site of 3D perovskite to form 2D perovskite phases, which can further improve the performance of tin-based PSCs due to the improved stability of 2D phases.[13] Two main types of organic ligands have been successfully incorporated into Sn-based perovskite films, including ammoniums with flexible alkyls, such as ethanaminium,[14] hexan-1-aminium,[15] butane-1,4-diaminium,[16] and ammo-

---

[*] G. Feng, H.-L. Loi, T. Wang, W. Deng, Q. Wei, Prof. M. Li, Prof. F. Yan
Department of Applied Physics, The Hong Kong Polytechnic University, Hung Hom, Kowloon, Hong Kong SAR, 999077, P.R. China
E-mail: apafyan@polyu.edu.hk

G. Feng, J. He, Prof. J. Wang
Beijing National Laboratory for Molecular Sciences, CAS Key Laboratory of Organic Solids, Institute of Chemistry, Chinese Academy of Sciences, Beijing, 100190 China
E-mail: jizheng@iccas.ac.cn

Z. Guan, Prof. C.-S. Lee, Prof. Q. Zhang
Center of Super-Diamond and Advanced Films (COSDAF), Department of Chemistry, City University of Hong Kong, Kowloon Tong, Hong Kong SAR, 999077, P.R. China
E-mail: qiczhang@cityu.edu.hk

G. Feng
Key Laboratory of Luminescence and Optical Information, Ministry of Education, Institute of Optoelectronic Technology, Beijing Jiaotong University, Beijing 100044, P.R. China

Prof. Q. Zhang
Department of Materials Science and Engineering, City University of Hong Kong, Tat Chee Avenue, Kowloon Tong, Hong Kong SAR, 999077, P.R. China

Prof. F. Yan
Research Institute of Intelligent Wearable Systems, The Hong Kong Polytechnic University, Hung Hom, Kowloon, Hong Kong SAR, 999077, P.R. China

niums with rigid aromatic groups, such as the benzene-based aromatic alkylammonium: phenylmethanaminium,[17] 2-phenylethan-1-aminium (PEA)[13b,18] and its derivatives,[19] like fluoro-phenethylammonium (F-PEA),[19d] pentafluorophenoxyethylammonium.[19e]

Thiophene is a π-electron-excessive heterocycle with the lone-pair electrons of the sulfur atom incorporated into the aromatic system. Compared to benzene, thiophene possesses a bit smaller size and lower aromaticity, which plays a pivotal role as a fundamental building block in the field of organic electronics. Thiophene-based organic cations have been used as passivators or big spacers in low 2D/3D mixed perovskites in solar cells,[20] field effect transistors,[21] photodetectors,[22] and light-emitting diodes[23] in the past years. For lead-based PSCs, thiophene-based cation 2-thiophenemethylammonium (ThMA) was first used by Liu's group to form 2D perovskites with the component formula of $(ThMA)_2(MA)_{n-1}Pb_nI_{3n+1}$ (MA: CH_3NH_3, $n=3$) and a power conversion efficiency (PCE) over15 % was obtained.[20a] Then, several other thiophene-based bulky ammoniums were successfully inserted into perovskite lattice, leading to promising performance of 2D/3D mixed PSCs.[20d,24] However, the application of thiophene-based bulky ammoniums in tin-based PSCs has been rarely reported until now.

Herein, we synthesized a new organic molecular ammonium salt 2-(thiophen-3-yl)ethan-1-aminium iodide (3-TEAI). For comparison, we introduced 3-TEAI, 2-(thiophen-2-yl)ethan-1-aminium iodide (2-TEAI), and PEAI into $FASnI_3$ with different stoichiometric ratios to form 2D/3D mixed perovskite films. Inverted PSCs with a structure of ITO/Poly(3,4-ethylenedioxythiophene) polystyrene sulfonate (PEDOT:PSS)/perovskite/Indene-C60 bisadduct (ICBA)/Bathocuproine (BCP) /Ag were fabricated in a N_2-filled glovebox by an antisolvent method. The resultant devices show a champion PCE of 14.16 % when 3-TEA is introduced in the $FASnI_3$ with proper content, higher than those of 2-TEA and PEA-based devices, which show PCEs of 13.33 % and 10.71 %, respectively. The 3-TEA-based devices also demonstrate good stability, which can sustain about 90 % of initial efficiency in the glovebox for about 2000 hours without encapsulation. The promising effect of 3-TEA can be explained through the results of Density functional theory (DFT) calculations, which show the lowest hole effective mass and formation energy in the 3-TEA-based 2D perovskite compared with other 2D perovskites.

Results and Discussion

To investigate the efficacy of thiophene-based spacers in tin-based PSCs and their comparison with benzene-based counterparts, we introduced two thiophene-based organic cation isomers (2-TEA, 3-TEA) and one benzene-based cation, PEA, into tin-based perovskites, as illustrated in Figure 1a. The corresponding hydriodate salts, PEAI and 2-TEAI, were utilized as received from commercial sources. The novel compound 3-TEAI was synthesized through an acid-base neutralization reaction employing 2-(thiophen-3-yl)ethan-1-amine and hydriodic acid as reactants, followed by purification via recrystallization, and the yield exceeded 90 %. The proton nuclear magnetic resonance (H^1NMR) spectra are depicted in Figure S1. The molecular dipole moment of the three spacers was calculated using density functional theory (DFT), with the results illustrated in Figure 1a. Specifically, PEA, 2-TEA, and 3-TEA exhibit dipole moments of 13.30 D, 13.13 D, and 14.38 D respectively. The heightened polarity of 3-TEA leads to an elevated dielectric constant, potentially addressing the disparity between the organic spacer and inorganic layers within 2D perovskites. Consequently, this effect may reduce the exciton binding energy, thereby facilitating both exciton separation and charge transport in the resulting 2D perovskite structure.[25]

To explore the influence of organic spacers within the A-site of 2D perovskites, we fabricated thin films of 2D ($n=1$, $n=2$) perovskites by spin-coating precursor solutions containing SnI_2, FAI, and 3-TEAI, 2-TEAI or PEAI dissolved in a mixed solvent of *N,N*-dimethylformamide (DMF) and dimethyl sulfoxide (DMSO). The fabrication methodology is detailed in the Supporting Information. From the X-ray diffraction (XRD) results (Figure 1b,c), all the patterns exhibit typical (00 *l*) diffractions with well-defined (002) peaks and secondary diffraction peaks, reflect-

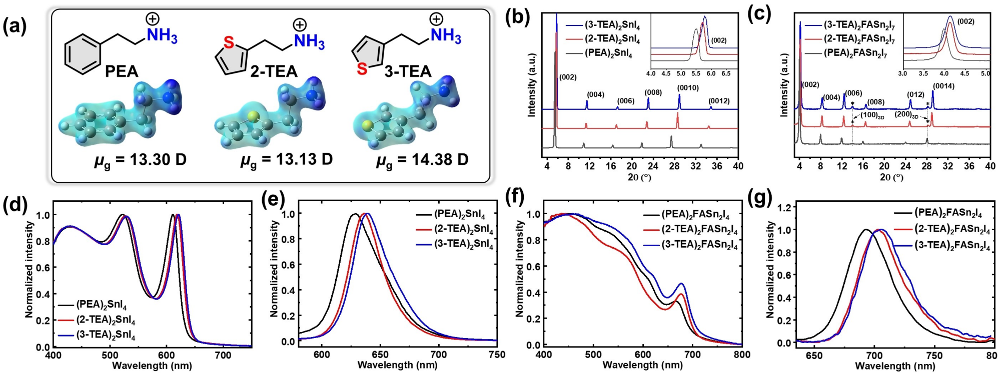

Figure 1. (a) Chemical structure, calculated electrostatic potential surface and dipole moment of PEA, 2-TEA, and 3-TEA. (b, c) XRD patterns, (d,f) UV/Vis absorption and (e, g) PL spectra of the 2D perovskite, (b, d, f) $n=1$, (c, e, g) $n=2$. Inset: (b,c) zoom in on the image of (002) peaks.

ing the ordered and layered crystalline structure inherent in the 2D perovskite films. Notably, the inset of Figure 1b illustrates a subtle increase in the (002) diffraction peak angle from 5.48° for $(PEA)_2SnI_4$, 5.70° for $(2\text{-}TEA)_2SnI_4$, to 5.77° for $(3\text{-}TEA)_2SnI_4$. This corresponds to a reduction in the spacing between two adjacent corner-sharing $[SnI_6]^{4-}$ octahedra layers reduced from 16.1 Å to 15.5 Å and 15.3 Å, respectively. This trend is consistent with findings from prior studies.[26] The presence of alkyl chains at distinct positions on the thiophene ring in 3-TEA diminishes steric hindrance relative to 2-TEA, thereby resulting in a slightly narrower interlayer spacing within the 2D perovskite structure. However, as the number of layers in the 2D perovskite increases to two ($n=2$), the difference in interlayer spacing between the 2-TEA and 3-TEA-based perovskites becomes less pronounced. The diffraction peaks for both 2-TEA and 3-TEA are very similar, occurring around 4.12°, yet still significantly larger than that of the PEA-based perovskite, as shown in Figure 1c. This indicates that as the spacer content in the perovskite decreases, the influence of TEA with different alkyl chain positions on the perovskite structure diminishes. UV/Vis absorbance and photoluminescence spectra (Figure 1d–g) further elucidate the influence of spacer cations on the photophysical properties of the 2D perovskites. Notably, compared to PEA-based 2D perovskites, the absorption and emission peaks exhibit a systematic red-shift progression, following the order of PEA < 2-TEA < 3-TEA.

To investigate the energy level disparities of the perovskites, we conducted ultraviolet photoelectron spectroscopy (UPS) measurements on the perovskite films deposited on ITO substrates. Integrating these results with the optical energy band gap (Eg) derived from absorption spectra, as shown in Figure S2–3 and Table S1, the schematic energy level diagrams were illustrated in Figure S4. Upon comparison of the valence band maximum(VBM) and conduction band minimum (CBM) energy levels among the 2D perovskites and the 3D counterparts $FASnI_3$. Almost all the energy levels of the thiophene-based 2D PVKs are higher than that of PEA-based PVKs, both in $n=1$ and $n=2$ configurations, this observation may be attributed to the stronger electron-donating ability of thiophene compared to benzene. All the CBMs of the 2D perovskites are higher than that of $FASnI_3$. However, compared to the 3D PVK, the $n=1$ PVKs show lower VBM and the $n=2$ PVKs show higher VBM. Therefore, the alignment of $n=2$ and 3D PVK could facilitate the formation of a type-II energy level structure in such 2D/3D heterostructures, which is conducive to hole extraction and augments electron barriers.

To investigate the impact of the 2D spacers in 2D/3D mixed perovskites across different compositional ratios, we prepared perovskite films by a spin-coating and antisolvent method, employing precursors with the formula of $L_xFA_{(1-x)}SnI_3$ where L represents the organic cation (PEA, 2-TEA, 3-TEA) and x denotes the molar fraction (ranging from 0 to 0.25). The detailed fabrication protocol is described in the Supporting Information. Subsequently, the XRD analyses were conducted on the films, with the resultant data elucidated in Figure 2. Analyzing the evolution of the diffraction pattern as a function of content ratio variation, the reference film ($x=0$) displays prominent peaks at 13.99°, 24.43°, 28.28°, and 31.71°, corresponding to the characteristic crystalline planes of (100), (102), (200), and (122) in 3D $FASnI_3$ crystal lattice.[18] Upon substitution of FA with larger organic spacers, the intensity of peaks at (100) and (200) significantly amplifies, while those corresponding to (102) and (122) gradually diminish, suggesting that the introduction of PEA, 2-TEA, or 3-TEA promotes oriented growth of the 3D perovskite perpendicular to the substrate, thereby enhancing carrier transport. Upon replacing 10 % of FA with the respective cations ($x=0.1$), no discernible new diffraction peaks emerge at lower angles. However, as the ratio increases to 15 % and 20 %, only minor peaks (from 3.0° to 4.5°) arise within the lower-angle region, indicative of the presence of $n=2$ perovskite phase but no $n=1$ content.[18,27] However, at a spacer content ratio of 25 %, additional diffraction peaks spanning 5° to 6.3° manifest in the XRD patterns of 2-TEA and 3-TEA-based films, corresponding to the $n=1$ phase. This transition may mark a pivotal point in the photovoltaic performance of the

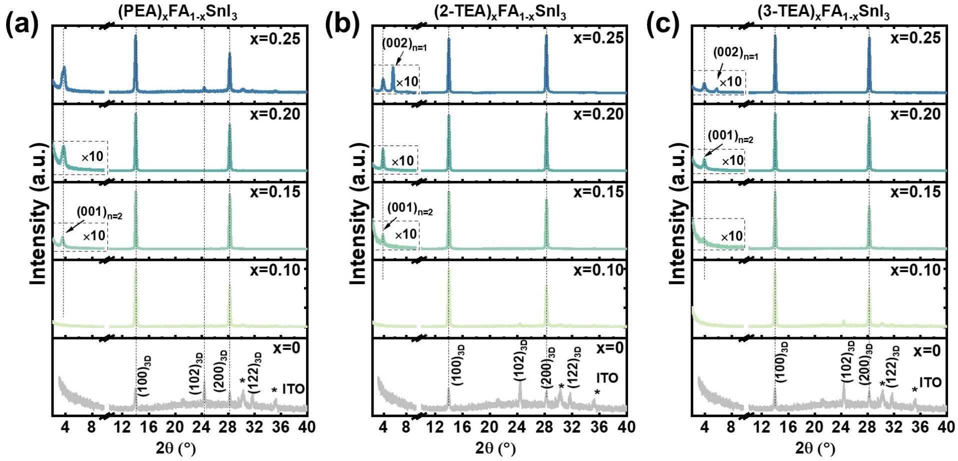

Figure 2. XRD patterns of the perovskite films with different contents (x) of (a) PEA, (b) 2-TEA, and (c) 3-TEA.

pertinent PSCs, as the quantum well structure of $n=1$ perovskites could impede carrier transmission, while the reduced content of the 3D phase may impact photoelectron generation. To further analyze the crystallinity, the full width at half maximum (FWHM) of the (100) diffraction peaks around 14° was calculated and plotted in Figure S5. The FWHMs exhibit a trend of initial decline followed by an increase as the content ratio of 2D spacers increases. Films based on 2-TEA and 3-TEA display the narrowest FWHM at a ratio of 0.2, while PEA-based films exhibit the narrowest FWHM at a ratio of 0.15. A narrower FWHM indicates superior crystalline properties, which are conducive to efficient photoelectric conversion in relevant PSC devices, particularly concerning the (100) peak representing 3D perovskite growth perpendicular to the substrate.

The morphological evolution of the 2D/3D perovskite films was assessed using scanning electron microscopy (SEM), as illustrated in Figure S6. The 3D $FASnI_3$ films exhibit densely packed grains of various shapes and sizes, with an average size of approximately 490 nm and a range from 160 nm to 1 μm, resulting in a rough surface texture. Upon incorporation of 10 % of PEA, 2-TEA, or 3-TEA into the 3D perovskite, the average grain sizes decrease to approximately 160 nm, 200 nm, and 230 nm, respectively. When the ratio is increased to 15 % and 20 %, the aforementioned distinct crystalline domains gradually disappear, yielding films with smoother and denser surfaces. However, at a ratio of 25 %, large flakes with numerous small pinholes appear on the film surface. When the concentrations of the three cations are equal, the impact of cation introduction on film morphology follows the order of PEA > 2-TEA > 3-TEA. Notably, at equivalent concentrations equal to or greater than 20 %, 3-TEA exhibits a superior morphology with reduced pinhole density.

To evaluate the influence of the 2D spacers on the photovoltaic performance of perovskite films. PSCs with an inverted planar configuration as ITO/PEDOT:PSS/Perovskite/BCP/ICBA/Ag (Figure 3a) were fabricated. Details of the device fabrication methods are described in the Supporting Information. 2D spacers could help inhibit the oxidation of Sn^{2+} to Sn^{4+} in 2D/3D mixed perovskite, but excessive 2D perovskite phase will reduce the optoelectronic properties. Here, we replace FA in $FASnI_3$ with different content (from 0 % to 25 %) of the 2D spacer PEA, 2-TEA, and 3-TEA, and obtain the perovskite films named $(PEA)_xFA_{(1-x)}SnI_3$, $(2\text{-}TEA)_xFA_{(1-x)}SnI_3$, $(3\text{-}TEA)_xFA_{(1-x)}SnI_3$, where $x=0$, 0.1, 0.15, 0.2 and 0.25). The Current density–Voltage (*J*–*V*) curves (forward scan) of the champion devices are shown in Figure 3b–d, and the device parameters are listed in Table S3–S5. The control devices based on $FASnI_3$ ($x=0$) show the best PCE of 6.87 %, along with open circuit voltage (V_{oc}) of 0.54 V, short circuit current (J_{sc}) of 20.27 mA cm^{-2}, and fill factor (FF) of 0.62. With the introduction of PEA, 2-TEA, and 3-TEA, all the devices exhibit enhanced J_{sc}, V_{oc}, and PCE, and the three highest PCEs of 10.71 %, 13.33 %, and 14.16 % were all obtained at the ratio of 20 % ($x=0.2$), respectively. To compare the repeatability of the devices without and different spacers, 30 individual devices of the four types of perovskite are carried out the related statistical parameter data are shown in Figure 3e–h. Accordingly, the

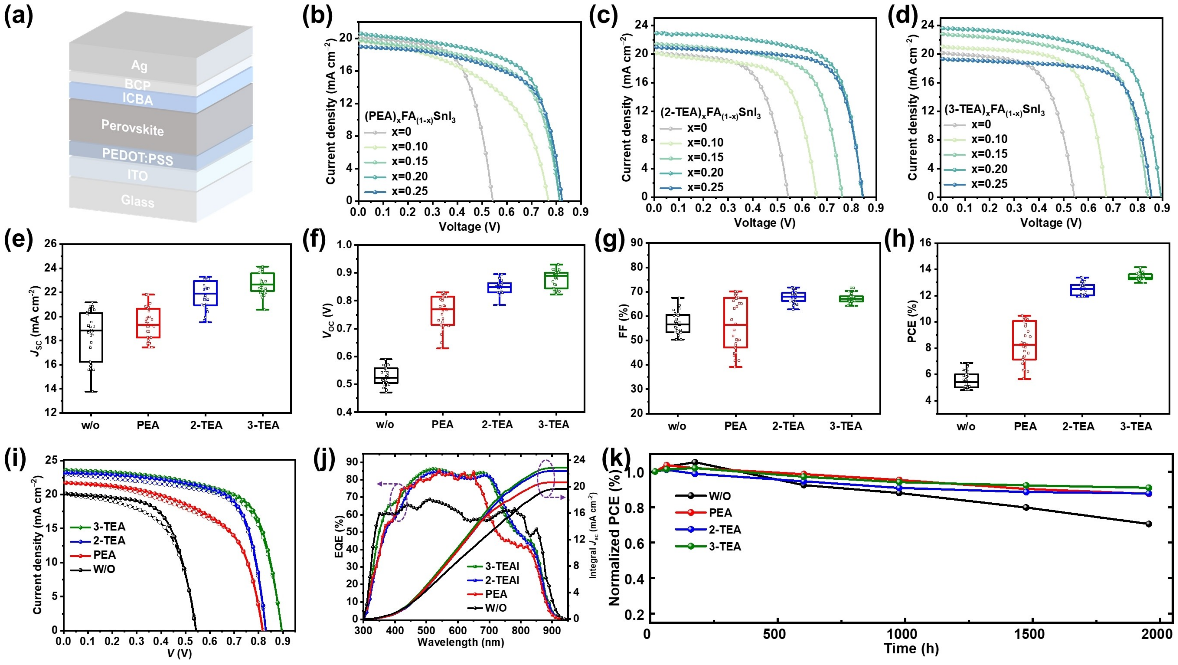

Figure 3. (a) Device architecture. (b–d) *J*–*V* curves of the champion devices of $FASnI_3$ and 2D/3D mixed perovskite with different content (x) of PEA, 2-TEA, and 3-TEA. (e–h) Statistics of the photovoltaic parameters including (e) J_{sc} (f) V_{OC}, (g) *FF* and (h) *PCE* of 30 devices for the tin-based PSCs without and with 20% PEA, 2-TEA, and 3-TEA. (i) *J*–*V* curves of the champion devices under forward (solid points) and reverse (hollow points) scans. (j) EQE spectra (solid points) and the integrated J_{sc} curves (lines) of the champion devices. (k) Normalized PCEs of the devices stored in a glovebox for over 1960 h without capsulation.

PCE of $FASnI_3$ devices varies from 4.81 % to 6.87 % with an average value of 5.54 %, while the PCEs of PEA, 2-TEA, and 3-TEA-based devices are gradually enhanced to the average value of 8.38 %, 12.52 % and 13.44 % with narrower distribution. The hysteresis is also effectively suppressed with the introduction of the 2D spacers, as shown in Figure 3i, the 3-TEA-based device shows the lowest hysteresis index.

Figure 3j shows the external quantum efficiency (EQE) spectrum of the related champion PSCs in the wavelength range from 300 to 900 nm, giving integrated J_{sc} of 19.67 mA cm^{-2} for $FASnI_3$ without 2D spacer, 20.70 mA cm^{-2}, 22. 41 mA cm^{-2}, and 22.88 mA cm^{-2} for the devices with PEA, 2-TEA, and 3-TEA, respectively, which are consistent well with the measured J_{sc} in J–V curves. And the light response range is also in line with the absorption spectra (Figure S7). The unpackaged devices were stored in the N_2-filled glovebox for about 1960 hours, after several times of device characterizations under illumination and exposure to the air, still maintained about 88 %, 88 %, and 91 % of the initial efficiency for PEA, 2-TEA, and 3-TEA-based devices respectively, which is much better than that of the $FASnI_3$-based 3D perovskite solar cells, only 70 % efficiency exist. Above all, the introduction of the 2D spacers with an appropriate amount could improve both the efficiency and the stability of the tin-based PSCs, while the spacers containing thiophene rings are more promising than those of benzene rings. Both the light soaking stability and thermal stability of the devices with 3-TEA were characterized as well. As shown in Figure S8, the device efficiency can maintain 80–85 % of its original value after continuous light soaking or heating for 40 hours. The performance degradation can be attributed to many factors, including the stability of both the perovskite, interfaces and charge transport layers, which should be further improved in the future.

To study how the 2D spacers influence the 2D/3D mixed PSCs' photovoltaic performance, it is essential to elucidate the microstructure of the perovskite films. Thus, grazing-incidence wide-angle X-ray scattering (GIWAXS) was employed to analyze the evolution of the perovskite crystal lattice across the depth of the films. The films of $(PEA)_{0.2}FA_{0.8}SnI_3$, $(2\text{-}TEA)_{0.2}FA_{0.8}SnI_3$ and $(3\text{-}TEA)_{0.2}FA_{0.8}SnI_3$ were subjected to the GIWAXS measurements at incident angles of 0.2°, 0.5° and 1.0° (corresponding X-ray penetration depths are about 50 nm, 150 nm, and 350 nm[19e,27]) to investigate the evolution of the perovskite crystal lattice from the surface to the bottom of the films. The resulting patterns and corresponding out-of-plane cutlines of the perovskite films are presented in Figure 4. All samples display distinct Bragg spots that can be indexed as the (100), (102), and (211) planes of the 3D perovskite $FASnI_3$ rather than the Debye–Scherrer rings. The intensity of these Bragg spots increases with higher incident angles, suggesting preferential orientation of the 3D perovskite phase, with the (100) plane oriented parallel to the substrate throughout the film thickness. PEA and 2-TEA-based

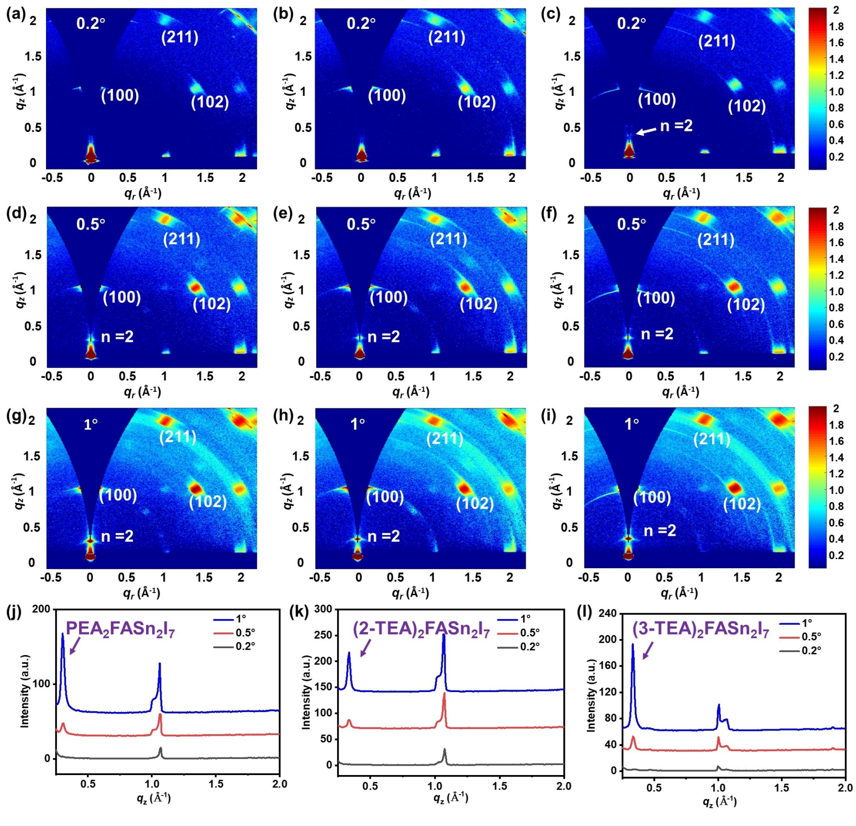

Figure 4. GIWAXS patterns (a-i) and out-of-plane cutlines (j-l) of the perovskite films deposited on ITO/PEDOT : PSS. (a, d, g, j) for $(PEA)_{0.2}FA_{0.8}SnI_3$, (b, e, h, k) for $(2\text{-}TEA)_{0.2}FA_{0.8}SnI_3$ and (c, f, i, l) for $(3\text{-}TEA)_{0.2}FA_{0.8}SnI_3$.

perovskite films exhibit no Bragg spots or Debye–Scherrer rings in the low q region (0.2 to 0.5 Å^{-1}) at the incident angle of 0.2°. However, a faint diffraction signal is detected in the out-of-plane direction of the pattern of 3-TEA-based film, indicating the presence of the 2D perovskite $(3\text{-TEA})_2FASn_2I_7$ only in the shallow surface of the $(3\text{-TEA})_{0.2}FA_{0.8}SnI_3$ films (Figure S9), which is beneficial to protect perovskites from oxidation. When the incident angle is 0.5°, Bragg spots at around 0.3 Å^{-1} become visible in the out-of-plane region for all three samples, and the diffraction intensity increases further at an incidence angle of 1°. This indicates the presence of the 2D ($n=2$) perovskite phase, oriented parallel to the substrate and distributed throughout the middle and bottom regions of the film. Comparing the intensities of the two primary sets of diffraction peaks in the out-of-plane direction (Figure 4j–l), we observe that the relative intensity of the diffraction peaks corresponding to the 2D phase of 3-TEA shows the greatest increase with the angle of incidence. This suggests that in the lower half of the films, the quantity of the 3-TEA-based 2D phase is higher than that of the PEA and 2-TEA-based 2D phase in the perovskite films. This could be further elucidated by the results of time-of-flight secondary ion mass spectrometry (TOF-SIMS), as depicted in Figure S10. Initially, the signal intensity of the cations of FA^+ and Sn^{2+} is on a high value and gradually diminishes to approximately one-half of the film depth, indicating similar trends. Subsequently, the FA^+ signal sharply decreases while the signal intensity of the 2D spacers enhances, signifying the emergence of the dimensional perovskite phase, primarily concentrated at the bottom part of the films. This observation is in agreement with the findings from GIWAXS analysis, which demonstrate the presence of a 2D perovskite phase in the lower half of all films of $(PEA)_{0.2}FA_{0.8}SnI_3$, $(2\text{-TEA})_{0.2}FA_{0.8}SnI_3$, $(3\text{-TEA})_{0.2}FA_{0.8}SnI_3$. Combining these results with the energy levels observed in the inverted devices (Figure S11), the intrinsic structure of the 2D/3D perovskite suggests a type-II band alignment, conducive to exciton separation and charge transport in inverted solar cells, thereby enhancing photovoltaic performance.

To delve deeper into the factors influencing the device performance of these perovskites, X-ray photoelectron spectroscopy (XPS) analysis was conducted on the perovskite films, with the corresponding spectra presented in Figure 5(a–d). The analysis reveals a significant oxidation state in the 3D perovskite, evidenced by a high content of 64.1 % for Sn^{4+}, nearly double that of Sn^{2+}. The elevated ratio of Sn^{4+} may be attributed to the exposure of the sample to air during transfer from the glove box to the XPS test chamber. In contrast, the 2D/3D mixed perovskites exhibit markedly lower proportions of Sn^{4+}, ranging from approximately 17.4 % to 12.3 %. This reduction highlights the effective passivation of the perovskite surface by the 2D spacers, thereby shielding it from oxidation. Notably, 3-TEA demonstrates the most effective performance in this regard. Time-resolved photoluminescence (TRPL) spectra were performed with perovskite films deposited on glass, to investigate the carrier lifetimes. And the decay lifetimes are obtained by fitting the spectra with a bi-exponential function, the results are shown in Figure 5e. $FASnI_3$'s carrier lifetime is only 21.6 ns while it's longer for all the 2D/3D mixed perovskites, as 33.5 ns for $(PEA)_{0.2}FA_{0.8}SnI_3$, 57.6 ns for $(2\text{-TEA})_{0.2}FA_{0.8}SnI_3$ and 67.4 ns for $(3\text{-TEA})_{0.2}FA_{0.8}SnI_3$. This indicates that the introduction of all three 2D spacers can extend the carrier lifetimes of the perovskite layers, and the 3-TEA shows performance better than 2-TEA and PEA, which is also consistent with the performance of the related devices.

The trap density of the perovskites was studied by the measurement of space charge limited current (SCLC) with the configuration of ITO/SnO_2/Perovskite/ICBA/BCP/Ag for electron-only devices and ITO/PEDOT:PSS/Perovskite/Poly[bis(4-phenyl)(2,4,6-trimethylphenyl)amine] (PTAA)/Au for hole-only devices, and the current–voltage curves

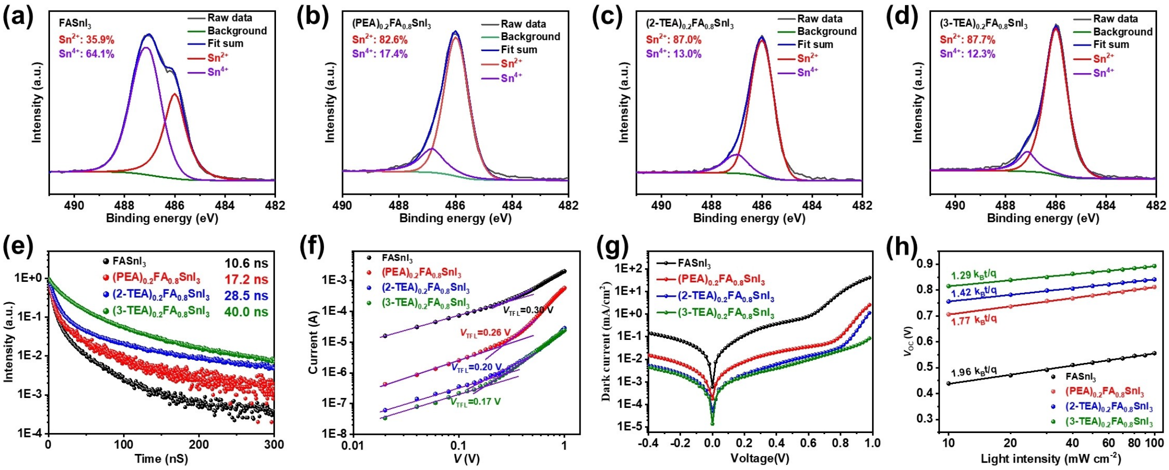

Figure 5. Sn 3d XPS of (a) $FASnI_3$ and (b) PEA, (c)2-TEA and (d)3-TEA based 2D/3D perovskite films on ITO. (e) TRPL spectra of the 3D perovskite and 3D/quasi-2D mixed perovskite films deposited on glass. (f) Dark *J–V* cures of the electron-only devices with the configuration of ITO/SnO_2/Perovskite/ICBA/BCP/Ag. (g) Dark *J–V* of the inverted solar cell devices. (h) The relationship of V_{oc} to the light intensity for devices based on the solar cell devices.

with double-logarithmic scale are tested under dark condition, the results are shown in Figure 5f and Figure S12. According to the slope of the curves, the ohmic regions are at low bias and the trap-filled limit voltage (V_{TFL}) is located on their onset voltage. Then the trap density (N_t) could be calculated with the equation of $N_t = \frac{2\ V_{\mathrm{TFL}}\ \varepsilon_r \varepsilon_0}{eL^2}$, where L is the film thickness of the perovskite (about 300 nm, from the cross-section SEM images, Figure S13), e is the elementary charge of one single electron, ε_0 is the vacuum permittivity, ε_r is the relative dielectric constant (35 for perovskites). The V_{TFL} of the electron-only devices for $FASnI_3$ and PEA, 2-TEA, 3-TEA-based 2D perovskites are measured at 0.30 V, 0.26 V, 0.20 V, and 0.17 V respectively, deducing the related N_t of about 3.44×10^{15} cm^{-3}, 2.98×10^{15} cm^{-3}, 2.29×10^{15} cm^{-3} and 1.95×10^{15} cm^{-3}. The V_{TFL} of the hole-only devices for the four films are 0.65 V, 0.51 V, 0.46 V, and 0.33 V, respectively, higher than those of the electron-only devices. The corresponding hole traps are 7.45×10^{15} cm^{-3}, 5.84×10^{15} cm^{-3}, 5.27×10^{15} cm^{-3}, and 3.78×10^{15} cm^{-3} for the four perovskite films, showing the same overall trend. Both experiments indicate alloying the 2D spacers into $FASnI_3$ could effectively reduce trap density, and the organic spacer 3-TEA shows a better ability to passivate the defect state than PEA and 2-TEA. To analyze the recombination of the carriers, dark J–V curves of the devices are measured as shown in Figure 5g. Compared to the 3D perovskite and PEA, 2-TEA-based devices (6.04×10^{-4} mA/cm^2, 1.82×10^{-4} mA/cm^2, and 5.19×10^{-5} mA/cm^2), 3-TEA-based devices shows the lowest saturation current density (1.39×10^{-5} mA/cm^2). This indicates the 3-TEA-based devices possess the lowest leakage current and charge carrier recombination. The V_{oc} measured under different light intensities are also plotted in Figure 5h, and the data were fitted to a line with a slope of $\frac{nk_BT}{q}$, where n is the ideality, q is the electric charge, k_B is the Boltzmann constant, and T is temperature. As a result, the device with 3-TEA shows an ideality factor of 1.29, which is lower than that of the devices prepared with PEA (1.42), 2-TEA (1.77), and 3D perovskites (1.96), indicating the 3-TEA's better ability to suppress the trap-assisted recombination than other two cations. This is also consistent with the better morphology and microstructure of the 3-TEA-based perovskite films than others. All these factors result in the best performance of 3-TEA-based PSCs.

DFT calculations were employed to delve deeper into the influence of organic cations on the properties of low-dimensional tin-based perovskites. Since the $n=2$ 2D perovskites are mainly located at the bottom of the 2D/3D perovskite films, in proximity and parallel to the PEDOT:PSS substrate, the hole mobility of the 2D perovskite is an important factor affecting the efficiency of the solar cell devices. Therefore, the hole-effective mass (m_h*) was calculated to compare the hole mobilities of the 2D perovskites. The models of the 2D perovskite were constructed and optimized, the crystal structures are shown in Figure S14–15. The structures of all 2D perovskites are anisotropic. The distances between two $[SnI_6]^{4-}$ octahedra layers of $(PEA)_2FASn_2I_7$, $(2\text{-}TEA)_2FASn_2I_7$, and $(3\text{-}TEA)_2FASn_2I_7$ are 11.35 Å, 11.07 Å and 11.06 Å respectively, which are consistent with the result of XRD. The hole-effective mass of the $n=2$ perovskites toward different directions (Γ-X, Γ-Y, and Γ-Z) was carried out by analyzing the curvature of the VBM near the Γ point. The calculated m_h* values are summarized in Table 1. The m_h*s of the perovskites toward Γ-X and Γ-Y are all much smaller than that towards Γ-Z, because of the large distance of the interlayer spacing along Z. However, when comparing the m_h* of the perovskite with different spacers in the same direction, the m_h* follows the trend of PEA >2-TEA >3-TEA, with the z-axis showing exponential differences (Table 1). All of this indicates that the $n=2$ 2D perovskite based on 3-TEA has higher mobility compared to those based on PEA and 2-TEA, in line with the trends observed in device performance.

The formation energy (E_{form}) of 2D perovskites ($n=2$) was also calculated from the optimized structures. As shown in Table 1, the result shows the E_{form} follows an order of 3-TEA < 2-TEA < PEA, which means the 3-TEA-based 2D perovskite possesses the highest structural stability. The high stability of a 2D perovskite layer can lead to improved capability to protect the 3D $FASnI_3$ perovskite from oxidation, which explains why the 3-TEA-based perovskite films show lower trap density than others. Moreover, the lower formation energy of 3-TEA-based perovskite can accelerate the crystallization process of the 2D perovskite phase and hence lead to the formation of a thin layer of $(3\text{-}TEA)_2FASn_2I_7$ layer in the shallow surface, which can improve the stability of the perovskite layer.

To better understand the minimal hysteresis observed in 3-TEA-based devices, which is related to ion migration in the perovskite, we conducted DFT simulations to model the iodide migration pathways within the unit cell of $n=2$ perovskites and calculate the corresponding activation energy, thereby verifying and comparing the effects of three different cations in the perovskites. Following established methods,[28] we simplified the migration process into five discrete steps in the simulation. Figures S16a-c depict the iodide ion‘s positions at the initial, middle, and final stages of migration, while Figure S16d summarizes the activation energies for each step. The trend in activation energies follows 3-TEA > 2-TEA > PEA, with values of 1.59 eV for $PEA_2FASn_2I_7$, 2.08 for $2\text{-}TEA_2FASn_2I_7$, and 2.33 eV for $3\text{-}TEA_2FASn_2I_7$ in the third step. These results indicate that iodide migration is most hindered in 3-TEA-based perovskites, followed by 2-TEA and PEA, supporting the role of 3-TEA in mitigating hysteresis in 2D/3D perovskite solar cells.

Table 1: The hole-effective masses along X, Y and Z direction and the formation energy of three different 2D perovskites.

2D Perovskite	m_h^* (m_e)			E_{form} (eV)
	Γ-X	Γ-Y	Γ-Z	
$(PEA)_2FASn_2I_7$	0.61	0.43	945.4	−2.98
$(2\text{-}TEA)_2FASn_2I_7$	0.60	0.40	236.3	−3.08
$(3\text{-}TEA)_2FASn_2I_7$	0.61	0.40	108.0	−3.13

Conclusions

In summary, we synthesized a novel thiophene-based cation, 3-TEA, and employed it as the spacer in 2D/3D tin perovskites, successfully integrating it into tin perovskite solar cells. Compared to its isomer, 2-TEA, and the conventional cation, PEA, 3-TEA exhibits the highest dipole moment and the lowest steric hindrance. Consequently, the 3-TEA-based 2D perovskite demonstrates the most compact crystal packing of $[SnI_6]^{4-}$ octahedral layers with the lowest hole-effective mass and formation energy. Replacing 20 % of FA in $FASnI_3$ with organic cations resulted in a 2D/3D mixed perovskite structure with enhanced crystallinity and orientation for all three spacers. This facilitated the formation of a type-II band alignment between the 3D and 2D perovskite, promoting hole extraction and charge transfer. Additionally, the 2D spacers demonstrated the ability to reduce defect density and suppress trap-assisted recombination within the 3D perovskite. Consequently, devices based on these perovskites exhibited significantly improved performance, with the highest PCE increasing from 6.87 % for $FASnI_3$ to 14.16 % for $(3\text{-TEA})_{0.2}FA_{0.8}SnI_3$. The thiophene-based devices also exhibit excellent stability, retaining approximately 90 % of their initial efficiency after storage in a glovebox for over 1960 hours without encapsulation. This study underscores the potential of thiophene-based organic cations, characterized by higher dipole moments, as promising candidates for fabricating high-performance tin perovskite solar cells.

Supporting Information

Supporting Information is available from the Wiley Online Library or from the author.

Acknowledgements

G.T. Feng, H. L. Loi and T. Y. Wang contributed equally to the work. This work is jointly supported by the Research Grants Council of Hong Kong, China (Project No. 15306822 and C1009-17EF) and the Hong Kong Polytechnic University, Hong Kong, China (ZE2X). This work is also supported by Shenzhen Science and Technology Innovation Commission (Project No. SGDX20210823103401011). The authors appreciate the financial support from the Hong Kong Scholars Program (Grant No. XJ2020051) and The RGC Postdoctoral Fellowship Scheme (RGC Ref. No. PDFS2324-5S03).

Conflict of Interest

The authors declare no conflict of interest.

Data Availability Statement

The data that support the findings of this study are available from the corresponding author upon reasonable request.

Keywords: lead-free · perovskite · solar cell · 2D spacer · thiophene

---

[1] a) A. S. R. Bati, Y. L. Zhong, P. L. Burn, M. K. Nazeeruddin, P. E. Shaw, M. Batmunkh, *Commun. Mater.* **2023**, *4*, 2; b) N. R. E. Laboratory, Best Research-Cell Efficiencies, https://www.nrel.gov/pv/cell-efficiency.html **2024**; c) H. Tang, Z. Shen, Y. Shen, G. Yan, Y. Wang, Q. Han, L. Han, *Science* **2024**, *383*, 1236–1240; d) B. Ding, Y. Ding, J. Peng, J. Romano-deGea, L. E. K. Frederiksen, H. Kanda, O. A. Syzgantseva, M. A. Syzgantseva, J.-N. Audinot, J. Bour, S. Zhang, T. Wirtz, Z. Fei, P. Dörflinger, N. Shibayama, Y. Niu, S. Hu, S. Zhang, F. F. Tiranito, Y. Liu, G.-J. Yang, K. Brooks, L. Hu, S. Kinge, V. Dyakonov, X. Zhang, S. Dai, P. J. Dyson, M. K. Nazeeruddin, *Nature* **2024**, *628*, 299–305.

[2] a) T. J. Macdonald, L. Lanzetta, X. Liang, D. Ding, S. A. Haque, *Adv. Mater.* **2023**, *35*, 2206684; b) J. Cao, F. Yan, *Energy Environ. Sci.* **2021**, *14*, 1286–1325; c) W. Yu, Y. Zou, H. Wang, S. Qi, C. Wu, X. Guo, Y. Liu, Z. Chen, B. Qu, L. Xiao, *Chem. Soc. Rev.* **2024**, *53*, 1769–1788.

[3] a) L. Lanzetta, T. Webb, J. M. Marin-Beloqui, T. J. Macdonald, S. A. Haque, *Angew. Chem. Int. Ed.* **2023**, *62*, e202213966; b) X. Jiang, Z. Zang, Y. Zhou, H. Li, Q. Wei, Z. Ning, *Accounts Mater. Res.* **2021**, *2*, 210–219.

[4] a) T. Wu, X. Liu, X. Luo, X. Lin, D. Cui, Y. Wang, H. Segawa, Y. Zhang, L. Han, *Joule* **2021**, *5*, 863–886; b) M. Zhang, Z. Zhang, H. Cao, T. Zhang, H. Yu, J. Du, Y. Shen, X.-L. Zhang, J. Zhu, P. Chen, M. Wang, *Mater. Today Energy* **2022**, *23*, 100891; c) A. Abate, *Joule* **2017**, *1*, 659–664.

[5] a) W. Liao, D. Zhao, Y. Yu, C. R. Grice, C. Wang, A. J. Cimaroli, P. Schulz, W. Meng, K. Zhu, R.-G. Xiong, Y. Yan, *Adv. Mater.* **2016**, *28*, 9333–9340; b) J. H. Heo, J. Kim, H. Kim, S. H. Moon, S. H. Im, K.-H. Hong, *J. Phys. Chem. Lett.* **2018**, *9*, 6024–6031.

[6] C.-M. Tsai, N. Mohanta, C.-Y. Wang, Y.-P. Lin, Y.-W. Yang, C.-L. Wang, C.-H. Hung, E. W.-G. Diau, *Angew. Chem. Int. Ed.* **2017**, *56*, 13819–13823.

[7] C. Wang, Y. Zhang, F. Gu, Z. Zhao, H. Li, H. Jiang, Z. Bian, Z. Liu, *Matter* **2021**, *4*, 709–721.

[8] Q. Tai, X. Guo, G. Tang, P. You, T.-W. Ng, D. Shen, J. Cao, C.-K. Liu, N. Wang, Y. Zhu, C.-S. Lee, F. Yan, *Angew. Chem. Int. Ed.* **2019**, *58*, 806–810.

[9] T. Wang, Q. Tai, X. Guo, J. Cao, C.-K. Liu, N. Wang, D. Shen, Y. Zhu, C.-S. Lee, F. Yan, *ACS Energy Lett.* **2020**, *5*, 1741–1749.

[10] Z. Lin, C. Liu, G. Liu, J. Yang, X. Duan, L. Tan, Y. Chen, *Chem. Commun.* **2020**, *56*, 4007–4010.

[11] T.-B. Song, T. Yokoyama, C. C. Stoumpos, J. Logsdon, D. H. Cao, M. R. Wasielewski, S. Aramaki, M. G. Kanatzidis, *J. Am. Chem. Soc.* **2017**, *139*, 836–842.

[12] M. E. Kayesh, T. H. Chowdhury, K. Matsuishi, R. Kaneko, S. Kazaoui, J.-J. Lee, T. Noda, A. Islam, *ACS Energy Lett.* **2018**, *3*, 1584–1589.

[13] a) H. Yao, S. Wang, Z. Jin, L. Ding, F. Hao, *J. Energy Chem.* **2023**, *77*, 144–156; b) F. Wang, X. Jiang, H. Chen, Y. Shang, H. Liu, J. Wei, W. Zhou, H. He, W. Liu, Z. Ning, *Joule* **2018**, *2*, 2732–2743; c) S. Shao, J. Liu, G. Portale, H.-H. Fang, G. R. Blake, G. H. ten Brink, L. J. A. Koster, M. A. Loi, *Adv. Energy Mater.* **2018**, *8*, 1702019.

[14] a) M. A. Kamarudin, D. Hirotani, Z. Wang, K. Hamada, K. Nishimura, Q. Shen, T. Toyoda, S. Iikubo, T. Minemoto, K. Yoshino, S. Hayase, *J. Phys. Chem. Lett.* **2019**, *10*, 5277–5283; b) K. Nishimura, M. A. Kamarudin, D. Hirotani, K. Hamada, Q. Shen, S. Iikubo, T. Minemoto, K. Yoshino, S. Hayase, *Nano Energy* **2020**, *74*, 104858; c) L. Xu, C. Zhang, X. Feng, W. Lv, Z. Huang, W. Lv, C. Zheng, G. Xing, W. Huang, R. Chen, *J. Mater. Chem. A* **2021**, *9*, 16943–16951.

[15] a) D. H. Cao, C. C. Stoumpos, T. Yokoyama, J. L. Logsdon, T.-B. Song, O. K. Farha, M. R. Wasielewski, J. T. Hupp, M. G. Kanatzidis, *ACS Energy Lett.* **2017**, *2*, 982–990; b) J. Wang, H. Shen, W. Li, S. Wang, J. Li, D. Li, *Adv. Sci.* **2019**, *6*, 1802019.

[16] P. Li, X. Liu, Y. Zhang, C. Liang, G. Chen, F. Li, M. Su, G. Xing, X. Tao, Y. Song, *Angew. Chem. Int. Ed.* **2020**, *59*, 6909–6914.

[17] J. Qiu, Y. Xia, Y. Zheng, W. Hui, H. Gu, W. Yuan, H. Yu, L. Chao, T. Niu, Y. Yang, X. Gao, Y. Chen, W. Huang, *ACS Energy Lett.* **2019**, *4*, 1513–1520.

[18] Y. Liao, H. Liu, W. Zhou, D. Yang, Y. Shang, Z. Shi, B. Li, X. Jiang, L. Zhang, L. N. Quan, R. Quintero-Bermudez, B. R. Sutherland, Q. Mi, E. H. Sargent, Z. Ning, *J. Am. Chem. Soc.* **2017**, *139*, 6693–6699.

[19] a) M. Y. Sun, M. Y. Ma, Y. Guo, S. Y. Yuan, H. Xiong, Z. Y. Tan, W. Z. Li, J. D. Fan, Z. J. Ning, *Solar RRL* **2022**, *6*, 2200672; b) P. Li, H. Dong, J. Xu, J. Chen, B. Jiao, X. Hou, J. Li, Z. Wu, *ACS Energy Lett.* **2020**, *5*, 2327–2334; c) M. Li, W.-W. Zuo, Y.-G. Yang, M. H. Aldamasy, Q. Wang, S. H. T. Cruz, S.-L. Feng, M. Saliba, Z.-K. Wang, A. Abate, *ACS Energy Lett.* **2020**, *5*, 1923–1929; d) B. B. Yu, Z. Chen, Y. Zhu, Y. Wang, B. Han, G. Chen, X. Zhang, Z. Du, Z. He, *Adv. Mater.* **2021**, *33*, e2102055; e) X. Meng, Y. Wang, J. Lin, X. Liu, X. He, J. Barbaud, T. Wu, T. Noda, X. Yang, L. Han, *Joule* **2020**, *4*, 902–912.

[20] a) H. Lai, B. Kan, T. Liu, N. Zheng, Z. Xie, T. Zhou, X. Wan, X. Zhang, Y. Liu, Y. Chen, *J. Am. Chem. Soc.* **2018**, *140*, 11639–11646; b) Y. Xu, K.-J. Jiang, P. Wang, W.-M. Gu, G.-H. Yu, X. Zhou, Y. Song, *New J. Chem.* **2022**, *46*, 2259–2265; c) T. Zhou, H. Lai, T. Liu, D. Lu, X. Wan, X. Zhang, Y. Liu, Y. Chen, *Adv. Mater.* **2019**, *31*, e1901242; d) D. Lu, G. Lv, Z. Xu, Y. Dong, X. Ji, Y. Liu, *J. Am. Chem. Soc.* **2020**, *142*, 11114–11122.

[21] a) S. Wang, S. Frisch, H. Zhang, O. Yildiz, M. Mandal, N. Ugur, B. Jeong, C. Ramanan, D. Andrienko, H. I. Wang, M. Bonn, P. W. M. Blom, M. Kivala, W. Pisula, T. Marszalek, *Mater. Horiz.* **2022**, *9*, 2633–2643; b) Y. Gao, Z. Wei, P. Yoo, E. Shi, M. Zeller, C. Zhu, P. Liao, L. Dou, *J. Am. Chem. Soc.* **2019**, *141*, 15577–15585; c) S. Wang, K. Bidinakis, C. Haese, F. H. Hasenburg, O. Yildiz, Z. Ling, S. Frisch, M. Kivala, R. Graf, P. W. M. Blom, S. A. L. Weber, W. Pisula, T. Marszalek, *Small* **2023**, *19*, 2207426; d) Z. Wei, K. Wang, W. Zhao, Y. Gao, Q. Hu, K. Chen, L. Dou, *Chem. Commun.* **2021**, *57*, 11469–11472.

[22] L. Jiang, Z. Li, Q. Dong, X. Rong, G. Dong, *ACS Appl. Mater. Interfaces* **2023**, *15*, 32647–32655.

[23] a) D. Han, J. Wang, L. Agosta, Z. Zang, B. Zhao, L. Kong, H. Lu, I. Mosquera-Lois, V. Carnevali, J. Dong, J. Zhou, H. Ji, L. Pfeifer, S. M. Zakeeruddin, Y. Yang, B. Wu, U. Rothlisberger, X. Yang, M. Grätzel, N. Wang, *Nature* **2023**, *622*, 493–498; b) Z. Wang, F. Wang, B. Zhao, S. Qu, T. Hayat, A. Alsaedi, L. Sui, K. Yuan, J. Zhang, Z. Wei, Z. a Tan, *J. Phys. Chem. Lett.* **2020**, *11*, 1120–1127; c) H. Jia, H. Shi, R. Yu, H. Ma, Z. Wang, C. Zou, Z. a Tan, *Small* **2022**, *18*, 2200036.

[24] a) C. Ni, Y. Huang, T. Zeng, D. Chen, H. Chen, M. Wei, A. Johnston, A. H. Proppe, Z. Ning, E. H. Sargent, P. Hu, Z. Yang, *Angew. Chem. Int. Ed.* **2020**, *59*, 13977–13983; b) Z. Xu, D. Lu, X. Dong, M. Chen, Q. Fu, Y. Liu, *Adv. Mater.* **2021**, *33*, 2105083; c) X. Dong, M. Chen, R. Wang, Q. Ling, Z. Hu, H. Liu, Y. Xin, Y. Yang, J. Wang, Y. Liu, *Adv. Energy Mater.* **2023**, *13*, 2301006; d) T. Zhou, H. Lai, T. Liu, D. Lu, X. Wan, X. Zhang, Y. Liu, Y. Chen, *Adv. Mater.* **2019**, *31*, 1901242.

[25] a) H. Zhang, R. Wang, L. Yang, Z. Hu, H. Liu, Y. Liu, *Angew. Chem. Int. Ed.* **2024**, *63*, e202318206; b) S. Tan, N. Zhou, Y. Chen, L. Li, G. Liu, P. Liu, C. Zhu, J. Lu, W. Sun, Q. Chen, H. Zhou, *Adv. Energy Mater.* **2018**, *9*, 1803024; c) H. Yao, T. Wu, C. Wu, L. Ding, Y. Hua, F. Hao, *Adv. Funct. Mater.* **2023**, *34*, 2312287.

[26] J.-T. Lin, C.-C. Liao, C.-S. Hsu, D.-G. Chen, H.-M. Chen, M.-K. Tsai, P.-T. Chou, C.-W. Chiu, *J. Am. Chem. Soc.* **2019**, *141*, 10324–10330.

[27] T. Wang, H.-L. Loi, J. Cao, Z. Qin, Z. Guan, Y. Xu, H. Cheng, M. G. Li, C.-S. Lee, X. Lu, F. Yan, *Adv. Sci.* **2022**, *9*, 2200242.

[28] S. Tan, I. Yavuz, N. De Marco, T. Huang, S.-J. Lee, C. S. Choi, M. Wang, S. Nuryyeva, R. Wang, Y. Zhao, H.-C. Wang, T.-H. Han, B. Dunn, Y. Huang, J.-W. Lee, Y. Yang, *Adv. Mater.* **2020**, *32*, 1906995.

Manuscript received: July 18, 2024
Accepted manuscript online: October 15, 2024
Version of record online: November 13, 2024